

Resonant double Auger decay in carbon *K*-shell excitation of CO

L. Journel, R. Guillemin, A. Haouas, P. Lablanquie, F. Penent, J. Palaudoux, L. Andric, and M. Simon
UPMC Université Paris 06, UMR 7614, Laboratoire de Chimie Physique Matière et Rayonnement, F-75005 Paris, France
CNRS, UMR 7614, Laboratoire de Chimie Physique Matière et Rayonnement, F-75005 Paris, France

D. Céolin

Department of Synchrotron Radiation Research, Lund University, Lund, SE-22100 Sweden

T. Kaneyasu

Institute for Molecular Science, Okazaki 444-8585, Aichi, Japan

J. Viehhaus and M. Braune

Fritz-Haber-Institut der Max-Planck-Gesellschaft, Faradayweg 4-6, D-14195 Berlin, Germany

W. B. Li,^{*} C. Elkharrat, F. Catoire, J.-C. Houver, and D. Dowek

Laboratoire des Collisions Atomiques et Moléculaires (LCAM), UMR 8625, Université Paris-Sud-CNRS, 91405 Orsay, France

(Received 8 February 2008; published 11 April 2008)

We have studied double Auger decay after $C\ 1s \rightarrow 2\pi^*$ photoexcitation in gas phase carbon monoxide. Two distinct processes, namely direct double Auger decay and cascade double Auger decay, are identified and studied in detail using multiple coincidence techniques. Cascade Auger decay is shown to be the overall dominant process. Decay channels involving the dissociation of the molecule followed by autoionization of the oxygen fragments are observed.

DOI: [10.1103/PhysRevA.77.042710](https://doi.org/10.1103/PhysRevA.77.042710)

PACS number(s): 33.80.Gj, 33.80.Eh, 33.15.-e, 33.20.-t

I. INTRODUCTION

In the soft x-ray energy range ($50\text{ eV} < h\nu < 1\text{ keV}$), inner-shell electrons of atoms and molecules can be promoted to unoccupied orbitals when the frequency of the incoming photon is tuned along discrete resonances, or ejected into the continuum when the photon energy exceeds the ionization potential. In both cases, a core hole is created leaving the system in a highly unstable state that relaxes either by radiative decay or Auger electron emission. For light elements ($Z < 26$), nonradiative decay is the dominant process after *K*-shell excitation [1]. Nonradiative decay can usually be described as a two-step process in which promotion of the inner-shell electron is followed by relaxation of the core-excited state and emission of an Auger electron. Auger decay leads primarily to the formation of singly charged species, when the system is photoexcited, or doubly charged ionic final states when the system is core ionized. However, using ion yield and electron spectroscopy, Carlson and Krause [2,3] showed that above threshold, more than one Auger electron can be emitted during the decay process leading to the formation of multiply charged ions (+3 or more), since in many cases the inner-shell ionization energy lies above multiple ionization threshold. Following this pioneering work, many studies on multiple Auger processes on rare gases have been reported. The most recent were based on electron-electron coincidence techniques [4–8].

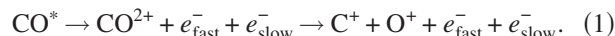
Double Auger emission may occur in two different ways. The two electrons produced during the decay of a core hole are ejected either simultaneously (direct double Auger) or sequentially in a cascade process. In the first case, the two Auger electrons share continuously the excess energy between the core-excited state and the final ionic state which is determined by the energy conservation principle, and electron correlation has to be considered to describe such a multielectron process. This energy sharing leads to a continuous distribution between the two Auger electrons with a pronounced preference for a U-shaped asymmetric energy sharing that corresponds to the emission of a slow and a fast Auger electron [6]. In the second case, the two electrons are emitted sequentially in a cascade Auger decay that gives rise to a structured energy spectrum. Each electron has a discrete energy that depends on the energy difference between the initial, intermediate, and final states. Both cases have been observed in rare gases. In particular, a direct double Auger has been evidenced in Ar *2p* [5,6] and Ne *1s* [6] core hole relaxation. For Xe *3d* [8,9], *4d* [4,7,8], Kr *3d* [8], and also Ar *2p* [10], a structured energy spectrum characteristic of a cascade Auger decay is prominent. Double electron emission has also been found in resonant Auger decay process in rare gases [11–13].

In the case of molecules, the situation can be more difficult to apprehend. Multiple Auger decay leads to the formation of multiply charged molecular ions, which are intrinsically unstable species. Ionic fragmentation and dissociation dynamics of multiply charged molecules have been extensively studied [14–18]. Using time-of-flight mass spectrometry and photoion-photoion coincidence techniques, it has been previously shown that CO molecules photoexcited along the $C\ 1s \rightarrow 2\pi^*$ resonance produce a significant yield

^{*}Present address: Hamburger Synchrotronstrahlungslabor HASY-LAB at Deutsches Elektronen-Synchrotron DESY, Notkestr. 85, D-22607 Hamburg, Germany.

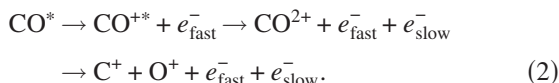
of doubly charged ionic fragments [19], therefore evidencing the occurrence of double Auger decay. Four channels have been identified, leading to the production of (a) $C^+ + O^+$, (b) CO^{2+} , (c) $C^{2+} + O$, and (d) $O^{2+} + C$, the dominant channel (about 80%) corresponding to the production of $C^+ + O^+$ [19].

Based on what is known for atoms, we can predict two distinct processes contributing to the double Auger decay of CO after $1s$ core-excitation or -ionization. The first one is a direct process in which the molecule relaxes by emitting simultaneously two electrons, producing doubly charged states of the parent molecules which eventually dissociate to C^+ and O^+ , or $C^{2+} + O$ or $O^{2+} + C$ following:

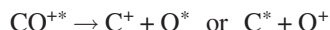


By analogy with atoms, one expects that the energy is shared between the two electrons leading to a continuous energy distribution with a maximum probability to have a fast Auger electron carrying most of the energy associated to a low energy Auger electron; therefore we use here already the notation e_{fast}^- and e_{slow}^- .

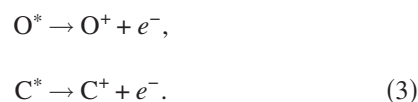
The second process is sequential. It starts with the excitation of the molecule and its relaxation by resonant Auger decay, followed by the emission of a second electron in a cascade process.



One electron is emitted at each step of the process and the energy sharing depends on the energy difference between singly charged intermediate CO^{*+} states and final electronic states involved. Excited CO^{*+} states can also dissociate prior to electronic emission as



followed by autoionization of the neutral (oxygen or carbon) fragment



For both processes (1) and (2), the final products are identical: two Auger electrons are emitted and one or two ions (CO^{2+} , $C^+ + O^+$, $C^{2+} + O$, or $C + O^{2+}$). Only the energy distribution of the two electrons allows us to distinguish between direct or sequential pathways.

The main difference with atoms is that the molecule may dissociate at any step of the process leading to more complex relaxation pathways than the simple one described above. The internuclear distance is an additional degree of freedom compared to the atomic case. In the case of CO, the $1s^{-1}2\pi^{*+1}$ core-excited state is bound [19] and ultrafast dissociation (faster than Auger decay) does not occur. However, if the singly charged ion is created in a dissociative excited state, it might be possible to observe the elongation of the chemical bond in the sequential process.

In this paper, we report the experimental results obtained on multiple Auger decay following resonant $C 1s^{-1}2\pi^{*+1}$ photoexcitation of isolated CO molecules by using different

experimental setups. Sequential and direct processes are both observed and discussed. The remainder of this paper is organized as follows. Section II summarizes the different experimental techniques we used. Section III introduces relevant spectroscopic data needed for the discussion of our data. Section IV is dedicated to the presentation of the results obtained and a related discussion. It is divided into two sections. The first one, Sec. IV A, presents the results obtained by electron-ion(-ion) coincidence measurements. The second one, Sec. IV B presents the results obtained by electron-electron coincidence measurements.

II. EXPERIMENT

Due to the difficulty in measuring simultaneously several particles (up to four in this study) in different kinetic energy ranges, we used three complementary coincidence experiments to investigate the energy and angular distributions of the emitted particles, ions, and electrons. We have used two different electron-ions coincidence experiments to measure the energy distribution of the electrons associated with the formation of the doubly charged CO^{2+} ion or $C^+ + O^+$, $C^{2+} + O$, or $O^{2+} + C$ ionic pairs. The first one is the vector correlation (VC) double velocity spectrometer [20,21]: it combines time-of-flight and imaging techniques and is adapted to the analysis of electrons and ionic fragments of comparable and relatively low energies ($E_{e,i} \leq 15$ eV). The second experiment, called EPICEA hereafter [22,23], combines a time-of-flight mass spectrometer with an electron analyzer dedicated to fast electron measurements. Finally, high-resolution electron-electron coincidences have been recorded with the HERMES experiment [24] which is based on a magnetic bottle time-of-flight (TOF) spectrometer.

A. Ion-ion-slow electron coincidence

The VC velocity spectrometer has been used to measure the ($\mathbf{V}_{C^+}, \mathbf{V}_{O^+}, \mathbf{V}_{e^-}$) velocity vectors for each (C^+, O^+, e^-) coincident event, corresponding to the dominant dissociative photoionization channel populated by double Auger decay of CO after $1s \rightarrow 2\pi^*$ resonant excitation at $h\nu = 287.4$ eV. Here \mathbf{V}_{e^-} is the initial velocity of one ‘‘slow’’ electron ($E_e \leq 15$ eV) and \mathbf{V}_{C^+} and \mathbf{V}_{O^+} are the velocities of the two ionic fragments. The ($\mathbf{V}_{C^{2+}}, \mathbf{V}_{e^-}$), ($\mathbf{V}_{O^{2+}}, \mathbf{V}_{e^-}$), and ($\mathbf{V}_{CO^{2+}}, \mathbf{V}_{e^-}$) velocity pairs for the three other channels populated by double Auger decay and leading to the production of a doubly charged fragment (C^{2+}), (O^{2+}) or parent ion (CO^{2+}), were simultaneously recorded. Experiments were performed on the bending magnet beamline SA22 at the Super-ACO positron storage ring (Orsay, France) and also on undulator beamline UE56/1-PGM-1 at BESSY (Berlin, Germany). Beamline SA22 provided photons in the 100–900 eV range with a resolving power up to 5000 and about 90% degree of linear polarization at the carbon $1s$ edge [25]. The experiment was done during the two-bunch operation mode of Super-ACO, providing a 120 ns period between light pulses and a pulse duration of $\delta t = 800$ ps. Beamline UE56/1-PGM-1 provides up to 1×10^{12} photons/s in the 60–1400 eV range with elliptical or linear polarization (100%) [26,27]

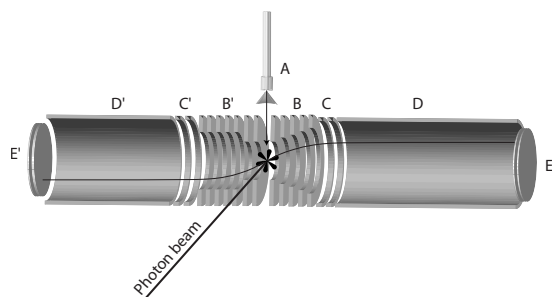


FIG. 1. Sketch of the double-velocity spectrometer. A: supersonic molecular beam. B and B': uniform field electrostatic electrodes (prime refers to the ion side). C and C': nonuniform field focusing lenses. D and D': equipotential flight tube. E and E': position sensitive detector.

and a resolving power of about 10 000 at the C *K* edge. The experiment was done during single bunch operation, providing a 800 ns period with a pulse duration of $\delta t = 50$ ps.

The VC double velocity spectrometer described in detail previously [20,21] was used in the electron-ion-ion coincidence mode [28]. Briefly, the interaction region is defined at the intersection of the photon beam and the molecular beam produced on the SAPHIRS setup [29], as schematized in Fig. 1. Electrons and ions are extracted from the interaction region in opposite direction by uniform electric fields (typically $\sim 100\text{--}150$ V cm $^{-1}$). The magnitude of the extraction field, combined with the use of two electrostatic lens sets (C and C' in Fig. 1) that focus the particle trajectories, significantly reduces broadening effects due to the finite dimensions of the interaction region and ensures the 4π collection of both particles (electrons and ions) for the studied processes. Both particles then fly through equipotential tubes D and D' before being detected by a position sensitive detector (PSD) (E and E'). This spectrometer provides for each event the impact position and TOF for each particle: (X_i, Y_i, T_i) and (X_e, Y_e, T_e) . Selection of the double Auger decay channels listed above is based on the ion TOF information. (C^+, O^+, e^-) events are selected in the TOF $_1$ -TOF $_2$ bidimensional histogram of the (ion_1, ion_2, e^-) events as described previously [28], whereas selection of the (C^{2+}, e^-) , (O^{2+}, e^-) , or (CO^{2+}, e^-) channels relies on the one-dimensional ion TOF spectrum corresponding to the events where a single ion is detected in coincidence with one electron. For the (C^+, O^+, e^-) channel, the conservation of momentum along the *x* and *y* axes in the dissociation process $CO^{2+} \rightarrow C^+ + O^+$ is used to correct the events for the remaining spatial extension of the target and to discriminate the events produced in the supersonic expansion from those arising from the minor thermalized component [28]. The three components of the emission velocity vector of each particle are then determined from the (X, Y, T) triplets, leading to the $(\mathbf{V}_{C^+}, \mathbf{V}_{O^+}, \mathbf{V}_{e^-})$, $(\mathbf{V}_{C^{2+}}, \mathbf{V}_{e^-})$, $(\mathbf{V}_{O^{2+}}, \mathbf{V}_{e^-})$, and $(\mathbf{V}_{CO^{2+}}, \mathbf{V}_{e^-})$ correlations diagrams. The main observable reported in this paper is the electron-ion kinetic energy correlation diagram (KECD). The KECD is the bidimensional histogram of the events distributed as a function of the slow electron energy and the kinetic energy release (KER) of the ion fragments, equal to the sum of the kinetic energies of the two atomic fragments. Several

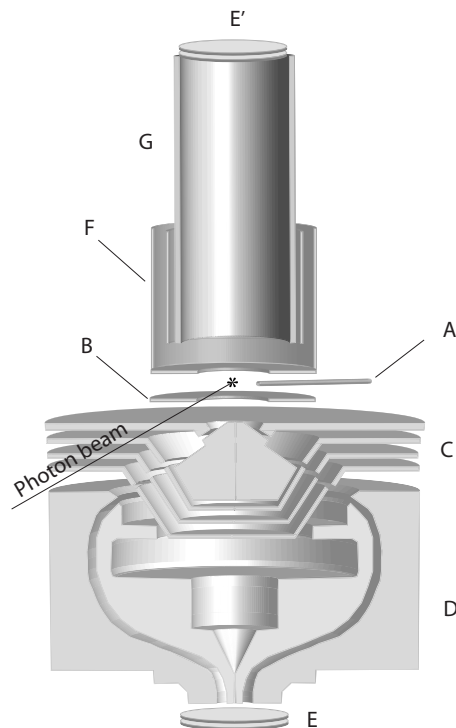


FIG. 2. Sketch of the EPICEA setup dedicated to Auger electron-ion-ion coincidences. A: gas inlet system providing a diffuse gas jet. B: extraction plate. C: focusing electrostatic lens for electrons. D: double toroidal analyzer. E (E' for ions): position sensitive detector. F: focusing lens for ions. G: field free flight tube.

electron and KER energy spectra derived from the KECDs provide information about the double Auger decay process, to be compared with those obtained from the two other techniques reported in the present paper. The $(\mathbf{V}_{C^+}, \mathbf{V}_{O^+}, \mathbf{V}_{e^-}, \hat{\mathbf{e}})$ vector correlation, where $\hat{\mathbf{e}}$ is the light quantization axis, as well as the other $(\mathbf{V}_{C^{2+}}, \mathbf{V}_{e^-}, \hat{\mathbf{e}})$, $(\mathbf{V}_{O^{2+}}, \mathbf{V}_{e^-}, \hat{\mathbf{e}})$, and $(\mathbf{V}_{CO^{2+}}, \mathbf{V}_{e^-}, \hat{\mathbf{e}})$ correlations also provide the molecular frame angular distribution (see Refs. [20,21]) of the slow Auger electrons. These results will be reported in a forthcoming paper.

B. Ion-ion-fast Auger electron coincidence

The energy distribution of the fast Auger electron has been obtained at the Swedish synchrotron radiation facility, MAX-Laboratory, on the undulator beamline I411. This beamline is equipped with a modified SX-700 monochromator which includes a 1220 l/mm grating and a plane-elliptical focusing mirror. It delivers 10^{11} to 10^{13} photons/s (depending on the resolution) in the 50–1500 eV energy range [30]. A typical resolving power of 5000 is achieved at the carbon *K* edge.

We used the EPICEA setup dedicated to Auger electron-ion-ion coincidence during multibunch operation. This setup has been already described in detail elsewhere [22,23]. Briefly, it consists of a double toroidal electron analyzer coupled to a TOF mass spectrometer both equipped with a PSD. Figure 2 shows a sketch of the setup. The monochromatized photon beam is focused onto an effusive gas beam

(A in Fig. 2) at the center of the extraction region. The working pressure in the chamber is kept at $\sim 10^{-5}$ Torr. The interaction region is kept field free (in order to preserve the kinetic energy (KE) resolution of the electron analyzer (around 1 eV in our experiment) until the detection of an electron triggers a pulsed field to extract the ions (B). Fast electrons are focused by a set of electrostatic lenses (C), optimized for high transmission [31], onto the entrance slit of an analyzer of double toroidal geometry (D). The angular acceptance of the electron analyzer is about 5% of 4π sr [22]. Electrons are detected on a PSD (E). The initial kinetic energy of the electrons is derived from the radius of impact of the electrons on the PSD. No correction for the transmission of the optics of the analyzer has been applied to our spectra. The pulsed extraction field (adjustable pulse height of a few hundreds of V/cm) applied on plate (B), after detection of an Auger electron as a trigger, allows the collection of all fragment ions. A focusing lens system is used for trajectory correction (F). The ions fly through a field free region (flight tube G), and are detected on a PSD (E'). We have measured coincidences either between the (CO^{2+}) or the (C^+, O^+) ions pairs and fast Auger electrons emitted during double Auger decay.

C. Electron-electron coincidence

Electron-electron coincidences were measured at high energy resolution using a magnetic bottle as a multielectron spectrometer. This apparatus, HERMES (high energy resolution multielectron spectrometer), was used on beamline UE56/2-PGM-1 [26,27] at BESSY, Berlin. The experiment was performed during single bunch mode of the synchrotron source (800 ns period) allowing for TOF measurements. The beamline delivers 10^{10} to 10^{12} photons/s in the 60–1500 eV energy range.

The TOF-PEPECO (time-of-flight-photoelectron-photoelectron coincidence) method has been detailed elsewhere [7]. The multielectron spectrometer used here is a smaller version (2.4 m instead of 5 m) of the one developed by Eland in Oxford [24]. Its principle is the measurement of electrons TOF in a magnetic bottle. Electrons are detected with a microchannel plate detector coupled to a multihit time-to-digital converter. Multicoincidences events between electrons are analyzed in energy after conversion of the time-of-flight. Figure 3 shows a sketch of the setup. The gas beam effusing from a 500 μm inner-diameter needle (A) crosses the monochromatized light beam at a right angle. The working pressure in the chamber is kept at $\sim 10^{-6}$ Torr to limit the count rate at a level where random coincidences remain negligible. A conical strong permanent magnet (0.7 T at contact, diameter=24 mm) is positioned with its pole close to the interaction region (B) with help of a 3-axis manipulator. The inhomogeneous field repels the electrons and parallelizes their trajectories, thus constituting a magnetic mirror for electrons. The electrons are then guided by a weak magnetic field (~ 1 mT) through the 2.4 m long solenoid (D) toward the detector. A double μ -metal layer (C) insures shielding from external magnetic fields. The electrons are detected on a stack of three microchannel plates (E). Essentially a 4π

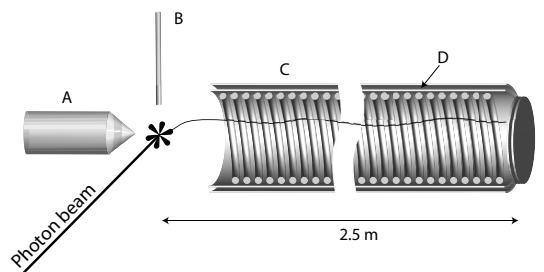


FIG. 3. Sketch of the magnetic bottle spectrometer. A: permanent conical magnet. B: hypodermic needle for sample gas introduction. C: 2.5-m-long solenoid. D: μ -metal shielding. E: microchannel plates.

solid angle collection is provided by the permanent magnet. The resolution was found to be $\Delta E/E=1\%$ to 2% .

III. SPECTROSCOPIC DATA ON CO MOLECULES

The electronic configuration of the CO ground state can be written as $(1\sigma)^2(2\sigma)^2(3\sigma)^2(4\sigma)^2(1\pi)^4(5\sigma)^2(2\pi)^0X^1\Sigma^+$. Figure 4 displays the orbital population of the CO molecular orbitals in terms of simple atomic contribution. The C 1s atomic core level corresponds to the (2σ) molecular orbital: excitation along the C $1s \rightarrow 2\pi^*$ resonance at $h\nu=287.4$ eV [19] creates a hole in the 2σ core orbital and promotes an electron into the lowest empty valence orbital 2π , leading to the configuration $(1\sigma)^2(2\sigma)^1(3\sigma)^2(4\sigma)^2(1\pi)^4(5\sigma)^2(2\pi)^1$.

Table I lists the threshold energies for the formation of CO^{2+} and $\text{C}^+ + \text{O}^+$ and other fragmentation channels as well as known thermochemical limits. Table II lists some of the

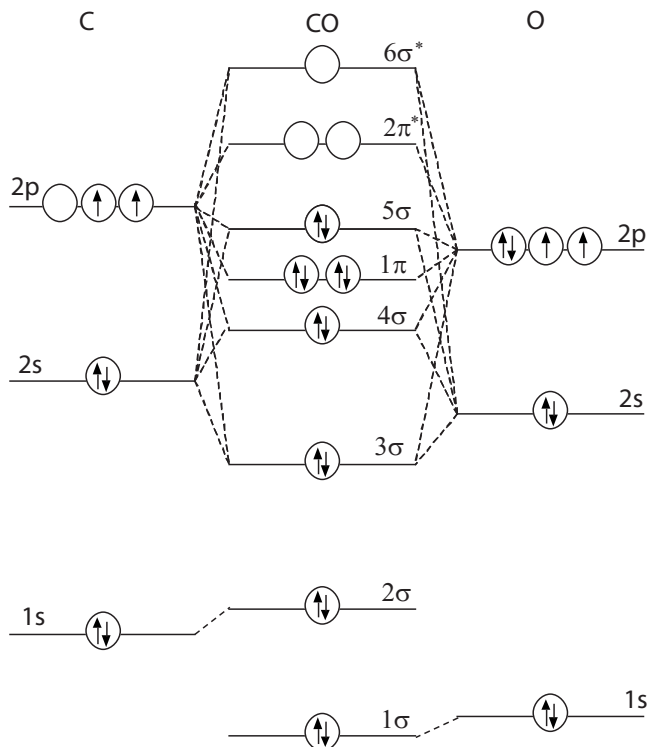


FIG. 4. Schematic of the molecular energy levels for CO.

TABLE I. Fragmentation channels and known thermochemical limits for the dissociation of the CO^{2+} dication.

Channel	Limit (eV) [32,33,35]
CO^{2+}	41.325
$\text{C}^{+(2P)} + \text{O}^{+(4S)}$	35.98
$\text{C}^{+(2P)} + \text{O}^{+(2D)}$	39.30
$\text{C}^{+(2P)} + \text{O}^{+(2P)}$	41.0
$\text{C}^{+(4P)} + \text{O}^{+(4S)}$	41.33
$\text{C}^{+(4P)} + \text{O}^{+(2D)}$	44.6
$\text{C}^{2+(1S)} + \text{O}^{(3P)}$	45.75
$\text{C}^{2+(1S)} + \text{O}^{+(4S)}$	59.36
$\text{C}^{(3P)} + \text{O}^{2+(3P)}$	59.87
$\text{C}^{+} + \text{O}^{2+(3P)}$	71.13
$\text{C}^{3+(2S)} + \text{O}^{(3P)}$	93.6

main electronics states of CO^{2+} known from calculations and measurements [34,36–39]. The energies from Refs. [34,36] were obtained at the neutral ground-state equilibrium internuclear distance ($R_{\text{C-O}}=1.128$ Å [34]) while values from Ref. [37] were obtained at equilibrium geometry for the C $1s$ core-excited state ($R_{\text{C-O}}=1.07$ Å [40]). It is important to note that most of the CO^{2+} states are populated differently by direct double photoionization or by Auger decay as discussed in [34].

The stability of the CO^{2+} dication is well-documented. Formation threshold energies for the four channels (a)–(d) (see below, Sec. IV A for definition of the channels) are reported in Table I. In particular threshold energies for channels (a) and (b) were found at 41.325 eV for CO^{2+} and 35.98 eV for $\text{C}^{+} + \text{O}^{+}$ thermodynamic threshold [34,35].

According to previous studies, CO^{2+} ions exhibit only a few quasistable levels [35,41]. The $\nu=0$ vibrational level of

 TABLE II. CO^{2+} dication electronic states and their energies in the Franck-Condon (FC) region relative to the CO ground state.

Symmetry	Configuration	Binding energy (eV)		
		Refs. [34,35]	Ref. [36]	Ref. [37]
$^3\Pi$	$(5\sigma)^{-1}(1\pi)^{-1}$	41.325	41.294	41.127
$^1\Sigma^{+}$	$(5\sigma)^{-2}$	41.525	41.700	40.861
$^1\Pi$	$(5\sigma)^{-1}(1\pi)^{-1}$	41.846	41.814	41.680
$^3\Sigma^{+}$	$(4\sigma)^{-1}(5\sigma)^{-1}$	42.5	43.573	42.927
$^3\Sigma^{-}$	$(1\pi)^{-2}$	44.4	–	44.956
$^1\Sigma^{+}$	$(4\sigma)^{-1}(5\sigma)^{-1}$	45.3	45.480	44.362
$^1\Delta$	$(1\pi)^{-2}$	46.5	–	46.804
$^3\Pi$	$(4\sigma)^{-1}(1\pi)^{-1}$	48.3	–	47.323
$^1\Sigma^{+}$	$(1\pi)^{-2}$	49.3	–	48.280
$^1\Pi$	$(4\sigma)^{-1}(1\pi)^{-1}$	50.7	–	50.080
$^1\Sigma^{+}$	$(4\sigma)^{-2}$	–	–	54.832
$^3\Sigma^{+}$	$(3\sigma)^{-1}(5\sigma)^{-1}$	–	–	62.321
$^3\Pi$	$(3\sigma)^{-1}(1\pi)^{-1}$	–	–	66.204
$^3\Sigma^{+}$	$(3\sigma)^{-1}(4\sigma)^{-1}$	–	–	68.279

 TABLE III. Autoionizing states of atomic oxygen from [48,49] and optical data from [50] (see also [51]). Electron energies are relative to the $\text{O}^{+(4S)}$ ground state of the ionic fragment.

Configuration		Electron energy (eV)
$2s^2 2p^3(^2D)3p$	3D	0.429
$2s^2 2p^3(^2D)3p$	3F	0.482
$2s^2 2p^3(^2P)3s$	3P	0.506
$2s^2 2p^3(^2P)3s$	1P	0.754
$2s^2 2p^3(^2D)3p$	1D	0.842
$2s^2 2p^3(^2D)3d$	3P	1.675
$2s^2 2p^3(^2D)3d$	3D	1.788
$2s^2 2p^3(^2D)4d$	$^3F, ^3D$	2.461

the $X^3\Pi$ (ground state) is quasistable with a lifetime $t > 3.8$ s. The lifetime of higher levels decreases dramatically as their energy increases and, 0.4 eV above the doubly charged ion ground state, there is no level with a lifetime greater than 0.1 μs . Within this 0.4 eV, there is only the $\nu=1$ level of the electronic ground state ($X^3\Pi$) and the $\nu=0$ level of the first electronic excited state ($^1\Sigma^{+}$). These two levels are degenerate within 0.1 eV and have a lifetime greater than 10 μs . As a consequence, we observe only a small amount ($\sim 4.5\%$) of CO^{2+} ions compared to the dominant $\text{C}^{+} + \text{O}^{+}$ channel ($\sim 82\%$). Under our experimental conditions, the CO^{2+} parent ions have a time of flight of about 2 μs . The electronic states of the dication lying above the $\nu=0$ levels of the $X^3\Pi$ and the $^1\Sigma^{+}$ states are unstable and decay by dissociation to the ground state $\text{C}^{+(2P)} + \text{O}^{+(4S)}$, through electronic predissociation by the dissociative $^3\Sigma^{-}$ state, and to the first excited state $\text{C}^{+(2P)} + \text{O}^{+(2D)}$ with the dissociation limit, respectively, at 35.98 and 39.30 eV [19,32,34,35] (see Table I).

Equation (2) describes a sequential double electron emission process involving CO^{+} electronic states. The CO^{+} ionic states to be considered in the studied reactions have binding energies above the $\text{C}^{+(2P)} + \text{O}^{+(4S)}$ lowest formation limit at 36 eV. Such one-hole (1h) and two-holes–one-electron (2h-1e) CO^{+} excited states have been assigned between 36 eV up to 60 eV, and correspond to, e.g., $(3\sigma)^{-1}$ or $(5\sigma)^{-1}(1\pi)^{-1}(2\pi)^{+1}$ electronic configurations [42–44]. The resonant Auger decay spectrum (not shown here, see [45] for instance) ranges from 12 eV up to 80 eV in binding energy and features the electronic states of CO^{+} , known from different measurements and calculations [40,42–47]. One-hole states (1h) and two-hole-one-electron states (2h-1e) have been well-identified up to the $^2\Sigma$ state lying at ~ 52.5 eV. The only identified electronic states lying in the 38–80 eV binding energy range are the $^2\Pi(5\sigma^{-1}1\pi^{-1}2\pi^{+1})$, $^2\Delta(3\sigma^{-1}1\pi^{-1}2\pi^{+1})$, and $^2\Sigma(5\sigma^{-1}1\pi^{-1}2\pi^{+1})$ states.

Following Eq. (3), it is possible to observe autoionizing states of an excited neutral fragment after dissociation of CO^{+} electronic states in $\text{C}^{+} + \text{O}^{*}$ or $\text{C}^{*} + \text{O}^{+}$. Table III gives the known autoionizing states of neutral oxygen extracted from [48–51] since this channel was dominantly observed in studies near double photoionization threshold [49].

IV. RESULTS

A. Ion-ion-electron coincidence

Using the VC method, four different channels corresponding to double Auger decay have been studied:

- (a) $h\nu + \text{CO} \rightarrow \text{C}^+ + \text{O}^+ + 2e^-$,
- (b) $h\nu + \text{CO} \rightarrow \text{CO}^{2+} + 2e^-$,
- (c) $h\nu + \text{CO} \rightarrow \text{C}^{2+} + \text{O} + 2e^-$,
- (d) $h\nu + \text{CO} \rightarrow \text{C} + \text{O}^{2+} + 2e^-$.

In the previous investigation by Hitchcock *et al.* [19], the ion-branching ratios between the double ionization channels (a)–(d) have been evaluated to (a) 78%, (b) 3%, (c) 12.5%, and (d) 6.25% (see Table IV of Ref. [19]). In the VC experiment we have used one-dimensional TOF spectra for selection of the (CO^{2+}, e^-) , (C^{2+}, e^-) , and (O^{2+}, e^-) events, and TOF₁-TOF₂ histograms for selection of the $(\text{C}^+, \text{O}^+, e^-)$, $(\text{C}^{2+}, \text{O}^+, e^-)$, and $(\text{C}^+, \text{O}^{2+}, e^-)$ events. Indeed, in order to achieve a meaningful characterization of channels (c) ($\text{C}^{2+} + \text{O}$) and (d) ($\text{O}^{2+} + \text{C}$) one must perform a weighted subtraction between the (C^{2+}, e^-) and (O^{2+}, e^-) events and those corresponding to the aborted triple ionization events for which an O^+ ion, or a C^+ ion, respectively, has not been detected due to the limited detection efficiency. Selection of these events leads to the measured relative branching ratios (a) 82%, (b) 4%, (c) 9%, and (d) 5%, the relative uncertainty on each value being of the order of 10%. We note that these numbers rely on a 4π collection of the two or three particles in the limits $E_e \leq 10$ eV, $E_{\text{C}^+ + \text{O}^+} \leq 10$ eV, and $E_{\text{C}^{2+} + \text{O}^{2+}} \leq 20$ eV. Beyond these limits the angular collection is progressively reduced. Taking this into account, the consistency with the data reported previously [19] is very satisfactory.

In the following we report in Secs. IV A 1 and IV A 2 the results obtained for the channels (a) and (b) using the VC method, and complementary results using the EPICEA setup concerning the production of high energy Auger electrons. The results for channels (c) and (d) are reported in Sec. IV A 3. The electron-electron coincidence results reported in Sec. IV B enlighten the discussion of the processes observed with the previous methods.

1. Channel (a): $\text{C}^+ + \text{O}^+$

The electron-ion kinetic energy correlation diagram (KECD) of the $(\text{C}^+, \text{O}^+, e^-)$ events corresponding to the dominant channel (a) displayed in Fig. 5(a) shows the distribution of the coincident events as a function of the electron energy E_e and the KER of the fragment ions. As mentioned above, a 4π collection of electrons and ions is achieved under the limits in energy $E_e \leq 10$ eV and $\text{KER} \leq 17.5$ eV. The KECD divides into two parts: region I corresponding to low KERs ($\text{KER} \leq 5.25$ eV) is weakly populated (about 4% of the events), whereas most events (96%) are found in the $5.25 \leq \text{KER} \leq 17.5$ eV region (II), which includes distinct structures. Figure 5 shows a detailed view of the $E_e \leq 7$ eV and $\text{KER} \leq 14$ eV region that contains most of the $(\text{C}^+, \text{O}^+, e^-)$ relevant features.

The structure identified in region I is characterized by a continuous ion fragment energy distribution with increasing intensity from 0 to 5 eV, and a well-defined electron energy $E_e \approx 0.5$ eV (FWHM ≈ 0.5 eV) [see Fig. 6(a)].

A small secondary electron peak is seen around 2 eV. The $E_e \approx 0.5$ eV energy peak has been observed in several studies of valence double photoionization below the adiabatic double ionization potential (for instance, [49,52] and references therein) and assigned to O^* atomic autoionization (see Table III): its production results from complete dissociation of a CO^{++} molecular ion followed by autoionization of the atomic oxygen fragment. In the TOF-PEPECO spectra reported in [49], several CO^{++} ionic states lying in the 36.4–40 eV binding energy region are vibrationally resolved when the O^* final state is identified and assigned to Rydberg states converging to the lowest CO^{2+} ionic states. Such states lead to KERs in the 0–3.4 eV range. We assign the structure in region I to a similar scheme [see Eq. (2)], where the CO^{++} molecular ion is produced by Auger relaxation of the $\text{CO}[(1s)^{-1}(2\pi^*)^{+1}]$ core excited molecule opened as soon as the decay CO^{++} state populated in the FC region lies above the ground state dissociation limit $\text{C}^+(^2P) + \text{O}^+(^4S)$ at 36 eV. This interpretation is supported by the electron-electron coincidence results reported in Sec. IV B.

The 0–5 eV KER distribution in region I is consistent with the production of CO^{++} ions in the 36–41.235 eV binding energy region dissociating into $\text{C}^+(^2P) + \text{O}^*(^3D, ^3F, ^3P)$ at about 36.5 eV. However it may *a priori* also involve CO^{++} ions lying above the $\text{CO}^{2+}(X^3\Pi)$ state that could dissociate, for instance, to $\text{C}^+(^4P) + \text{O}^*(^3D, ^3F, ^3P)$ limits lying at about 41.9 eV or to higher limits.

Region II of the KECD starts from KER values identified for the lowest dissociative CO^{2+} ionic states. The dominant structure labeled α has its maximum at ($E_e \approx 2$ eV, $\text{KER} \approx 6.5$ eV). The KER peak at 6.5 eV, populated for all E_e electron energies in the $0 \leq E_e \leq 10$ eV range [see Figs. 6(d)–6(f)], is well-resolved compared to the higher KER structures in Fig. 5(b). It can be assigned to the $\text{CO}^{2+}(^1\Pi, v=0, 9)$ electronic state [35,39,53] located in the 41.8–43 eV binding energy region. These states dissociate to the ground state limit $\text{C}^+(^2P) + \text{O}^+(^4S)$ at 36 eV. A contribution to peak α of the dissociative components of the lower $\text{CO}^{2+}(X^3\Pi, v \geq 3)$ and $\text{CO}^{2+}(^1\Sigma^+)$ electronic states populating the same limit cannot be excluded. The electron energy distribution associated to peak α , centered at $E_e \approx 2$ eV, is rather extended with a flat maximum lying from 1.5 to 2.5 eV and a full width at half maximum (FWHM) of 4 eV [see also Fig. 6(b)]. This width is significantly larger than the energy resolution which is 1.3 eV for 2 eV energy electrons. The vertical shape of peak α excludes a continuous energy sharing between the slow electron and the nuclei that would confer a diagonal shape to the electron-ion kinetic energy correlation peak. Therefore the electron energy width of peak α must be attributed to a local energy sharing between the fast and slow electrons that should in principle be observed in the electron-electron coincidence data (see Sec. IV B).

The characteristics of peak α are consistent with a two-step sequential decay where emission of a fast Auger electron populates one or several CO^{++} state(s) which then autoionizes to the $\text{CO}^{2+}(^1\Pi)$ state: the 4 eV width of the

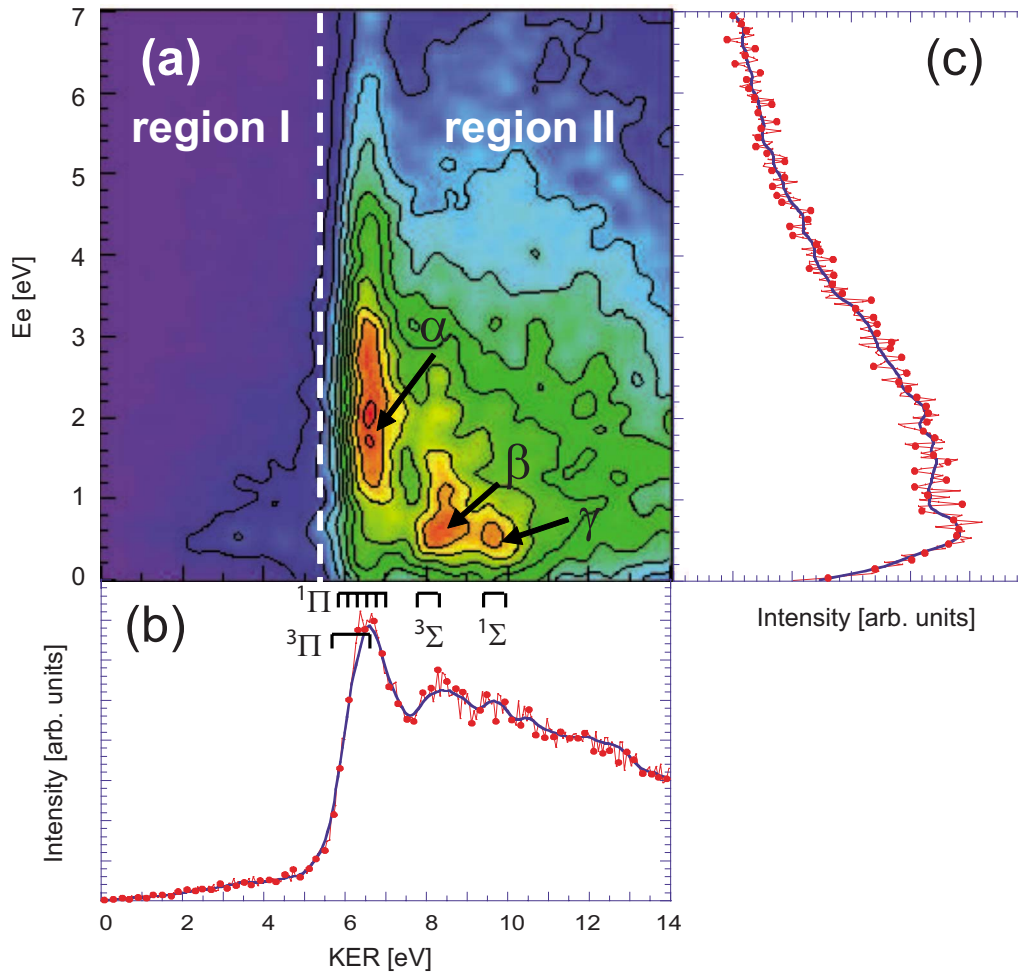


FIG. 5. (Color online) (a) E_e -KER kinetic energy correlation diagram (KECD) of the (C^+, O^+, e^-) events; region I (KER ≤ 5.25 eV) and region II ($5.25 \leq \text{KER} \leq 14$ eV) including structures α , β , and γ (see text); (b) total KER distribution, and (c) total electron energy distribution resulting from the projection of the KECD onto the horizontal and the vertical axis, respectively.

electron distribution suggests that the intermediate CO^{**} states must either be strongly repulsive in the FC region or correspond to a dense series, centered in the 44 to 45 eV binding energy region above the CO ground state. In the deexcitation spectrum (DES) of Eberhardt *et al.* [42], this binding energy region corresponds to the prominent 4 eV broad peak D_4 (FWHM) assigned to spectator Auger decay to two-hole-one-electron (2h-1e) satellite states of $(3\sigma)^{-1}(5\sigma)^{-1}(2\pi)^{+1}$ dominant configuration, consistent with multichannel Schwinger configuration interaction calculations [43]. Therefore we assign peak α to molecular autoionization of spectator Auger decay satellite CO^{**} states populated in the 42–47 eV binding energy region (D_4), into the dissociative components of $\text{CO}^{2+}(^1\Pi)$ [$\text{CO}^{2+}(X^3\Pi, v \geq 3)$ and $\text{CO}^{2+}(^1\Sigma^+)$] electronic state(s).

Although the electron energy spectrum for the 6.5 eV KER is dominated by the α structure discussed above, the detailed shape of the electron energy distribution in Fig. 6(b) indicates a contribution from other processes since, for instance, a relative maximum may be inferred for $E_e \approx 0.5$ eV. In Figs. 6(a)–6(c), the reported electron energy spectra correspond to an additional $60^\circ \leq \theta_z \leq 120^\circ$ angular selection of electrons emitted about a plane perpendicular to

the spectrometer axis z . This procedure allows us to extract events with improved electron energy resolution, whereas the relative importance of the structures is unchanged due to the rather isotropic angular distribution of the electrons in the laboratory frame ($\beta_e \approx -0.2$). Finally, we observe a low intensity tail extending to $E_e \approx 10$ eV which suggests the contribution of an underlying continuous energy distribution that can be assigned to direct double Auger decay leading to the population of the $\text{CO}^{2+}(^1\Pi)$, $\text{CO}^{2+}(X^3\Pi, v \geq 3)$, and/or $\text{CO}^{2+}(^1\Sigma^+)$ states.

Two other structures in the KECD, Figs. 5(a) and 6(d), β and γ , whose maxima correspond to larger KERs, partially resolved at about 8.3 and 9.5 eV, and a smaller electron energy, $E_e \approx 0.5$ eV, are identified in the KECD. A secondary maximum ($E_e \approx 1.5$ eV) is seen in the electron energy distribution corresponding to the 8.3 eV KER [β' in Figs. 6(c) and 6(e)]. These KERs (β and γ structures) may be assigned to the $\text{CO}^{2+}(1^3\Sigma^+)$ and $\text{CO}^{2+}(2^1\Sigma^+)$ electronic states dissociating to the ground state limit $C^+(^2P) + O^+(^4S)$ at 36 eV [35,39,53], lying at 43.8–44.3 eV and 45.5–45.8 eV binding energies, respectively. The E_e -KER energy correlation corresponding to β and γ favors the interpretation of these structures as due to molecular autoionization of CO^{**}

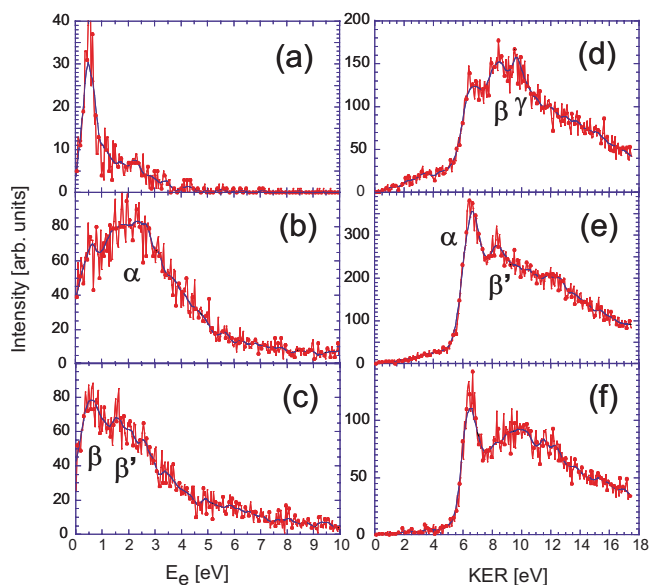


FIG. 6. (Color online) Energy distributions extracted from the complete KECD corresponding to Fig. 5; intensities are in arbitrary but consistent units. Electron energy distributions for specific KER selections: (a) $0 \leq \text{KER} \leq 5.25$ eV, (b) $5 \leq \text{KER} \leq 7.5$ eV, and (c) $7.5 \leq \text{KER} \leq 9.3$ eV, with additional angular selection of electrons emitted about a plane perpendicular to the spectrometer axis z (see text); KER distributions for specific energy selections: (d) $0 \leq E_e \leq 1$ eV, (e) $1 \leq E_e \leq 3$ eV, and (f) $5 \leq E_e \leq 7$ eV.

states populated by Auger decay at 44.3–44.8 eV and 46–46.3 eV binding energies, also corresponding to the D_4 peak in the DES spectrum [42]. We do not exclude at this point the underlying contribution of 0.5 eV electron emission due to the autoionization of the oxygen atom as discussed above [see Eq. (2)]. A CO^{+*} state lying, for instance, at 45 eV binding energy (maximum of peak D_4) and dissociating to the $\text{C}^+(^4P) + \text{O}^*(^3D, ^3F, ^3P)$ limits would indeed involve typically a KER of 8.5 eV. It is unlikely that such a CO^{+*} state would have a well-defined energy leading to the observed structures. However, a broader KER distribution corresponding to the population of dissociative repulsive CO^{+*} ionic states might contribute to the $E_e \approx 0.5$ eV line. This possibility is supported by the electron-electron coincidence observations (see Figs. 13 and 14 and related discussion). For KERs larger than 10 eV and electron energies outside the structures discussed above, the energy distribution of the $(\text{C}^+, \text{O}^+, e^-)$ events in the KECD is rather continuous, significantly decreasing as the KER and/or the electron energy increase as seen in Fig. 6. These events may be attributed to higher binding energy regions which may *a priori* involve Auger decay to CO^{+*} highly excited states, followed by ionization to CO^{2+} dissociative states and/or direct double Auger decay to CO^{2+} repulsive ionic states, characterized by a quasicontinuous electron energy sharing between the fast and slow electrons. We note that the structures discussed above are smeared out in the E_e total energy distribution corresponding to the projection of the 2D KECD onto the E_e vertical axis of Fig. 5(c), which illustrates the overall decreasing low energy electron emission probability as a function of E_e . The total KER distribution resulting from the

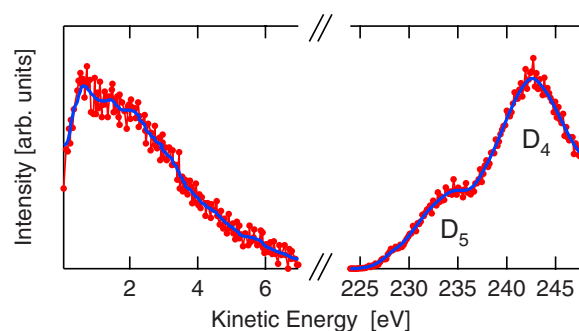


FIG. 7. (Color online) Energy distribution of the Auger electrons in coincidence with a $\text{C}^+ + \text{O}^+$ fragment.

projection of the KECD onto the horizontal axis of Fig. 5(b) remains structured. The energy resolution in the KER spectrum is significantly enhanced with respect to previously reported KER energy distributions in photoion-photoion-coincidence (PIPICO) measurements [19,54] at the same photon energy, although the envelopes of the spectra have comparable shapes. As discussed above, the structures with maxima observed at 6.5, 8.3, and 9.5 eV are assigned to the population of the $\text{CO}^{2+}(^1\Pi)$ [which partially overlaps with $\text{CO}^{2+}(X^3\Pi)$ and $\text{CO}^{2+}(^1\Sigma^+)$ states], $\text{CO}^{2+}(1^3\Sigma^+)$, and $\text{CO}^{2+}(2^1\Sigma^+)$ states, respectively. We cannot exclude a contribution from other CO^{2+} ionic states because of the large density of states lying in the same binding energy region [32]. In order to emphasize this comparison, we recall that the spectrum in Fig. 5(b) is the KER distribution for the $(\text{C}^+, \text{O}^+, e^-)$ events in the relevant $\text{KER} \leq 14$ eV region, with the restriction that the slow electron collection is complete only for $E_e \leq 10$ eV (excluding events corresponding to less asymmetric energy sharing between the two escaping electrons), although previous results characterize *a priori* the whole (C^+, O^+) events. Finally the measured KER spectrum at the $1s \rightarrow 2\pi^*$ resonance ($h\nu = 287.4$ eV) is significantly different from that obtained above ionization threshold (not shown here), which shows the dominant contribution of KERs assigned to the production of the $\text{CO}^{2+}(^1\Pi)$ and $\text{CO}^{2+}(2^1\Sigma^+)$ electronic states, and a weaker contribution from the $\text{CO}^{2+}(1^3\Sigma^+)$ [53].

The spectrum displayed in Fig. 7 shows the energy distribution of the fast and slow Auger electrons measured in coincidence with the $\text{C}^+ + \text{O}^+$ ion pairs. The low energy part of the spectrum (0–16 eV), measured with the VC spectrometer is identical to the one reported in Fig. 5(c). The high energy part (225–250 eV) is obtained with the EPICEA spectrometer. It shows two structures, which correspond to D_4 (40–50 eV binding energy) and D_5 (50–60 eV binding energy) resolved peaks in the DES spectrum reported by Eberhardt *et al.* [42] which has been used for calibration. As discussed above peak D_4 has been assigned to spectator Auger decay into $2h-1e$ satellite CO^+ states with $(3\sigma)^{-1}(5\sigma)^{-1}(2\pi)^{+1}$ principal configurations [42,43], whereas D_5 is assigned to $(3\sigma)^{-1}(1\pi)^{-1}(2\pi)^{+1}$ and $(3\sigma)^{-1}(4\sigma)^{-1}(2\pi)^{+1}$ principal configurations [42]. Their attribution to the $(\text{C}^+ + \text{O}^+)$ channel is consistent with the previous discussion of the structures observed in the KECD and establishes the higher binding energy region assigned as D_5 does play a role in the production of the $(\text{C}^+ + \text{O}^+)$ channels.

TABLE IV. β asymmetry parameter for different KER selections indicated in the table between the brackets..

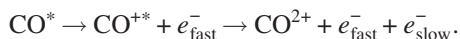
KER selection (eV)	$\beta_{C^+/O^+}(\pm 0.05)$
[0–5.25]	–0.75
[5–7.50]	–0.40
[7.5–9.30]	–0.70
[9.3–11.0]	–0.85
[11–17.5]	–0.95

For the five identified KER regions, we report for the sake of completeness the measured β ion fragment asymmetry parameters (see Table IV), while the electron asymmetry parameters in these selections is $\beta_e \approx -0.20(\pm 0.05)$. The β_{C^+/O^+} asymmetry parameters are consistent with those reported by Saito *et al.* [54] in the KER regions 4–8 eV ($\beta \approx -0.4$) and larger than 12 eV ($\beta \approx -0.95$). They evidence a breakdown of the axial recoil approximation for the dissociation of CO^{2+} ionic states corresponding to KERs below 10 eV, as also observed in molecular frame photoemission studies above the C 1s ionization threshold [53]. For the larger KERs, the $\beta_{C^+/O^+} \approx -1$ is consistent with the π symmetry of the $1s \rightarrow 2\pi^*$ transition, as long as the axial recoil approximation is valid.

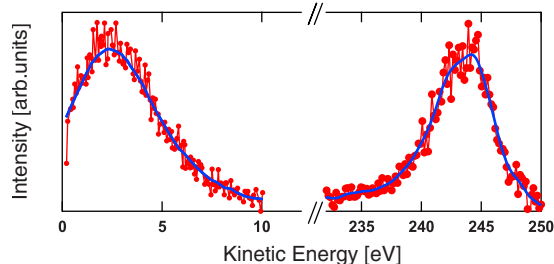
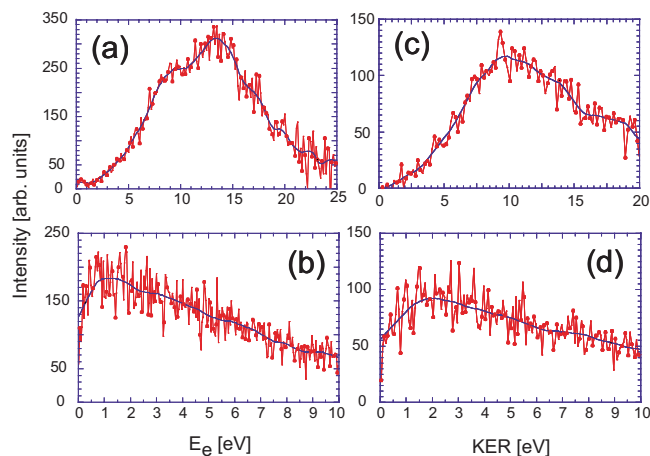
2. Channel (b): CO^{2+}

Figure 8 shows the electron kinetic energy distribution measured in coincidence with CO^{2+} ions, after resonant photoexcitation at $h\nu = 287.4$ eV. The low energy part of the spectrum (0–16 eV) is measured with the VC spectrometer, while the high energy part (234–250 eV) is obtained with EPICEA.

The low electron energy spectrum shows a broad distribution with a flat maximum at $E_e \approx 2$ eV, and about 5 eV width (FWHM). The quasistable states of CO^{2+} consist of the ground state $CO^{2+}(X^3\Pi, v=0,1)$ and the $CO^{2+}(^1\Sigma^+, v=0)$ levels, restricted in a 0.4 eV energy region (41.3–41.7 eV) (see Sec. III). Therefore channel (b) is attributed to a fast electron Auger decay to CO^{+*} ionic states lying in the 41.5–46.5 eV binding energy region centered about 43.5 eV (D_4 region in the DES spectrum [42]), followed by autoionization to CO^{2+} :



We identify the present reaction as the nondissociative component of process α . On the high-energy side, we observe a


 FIG. 8. (Color online) Electron energy spectrum corresponding to the production of CO^{2+} bound states.

 FIG. 9. (Color online) KER and electron energy spectra for reaction $C^{2+}+O$ [panels (a) and (b)] and for reaction $O^{2+}+C$ [panels (c) and (d)].

single peak with a maximum at ~ 244 eV of kinetic energy which is the counterpart of the low energy spectrum: it corresponds to CO^+ states of ~ 43 eV binding energy, 2 eV above the lowest $CO^{2+}(X^3\Pi, v=0,1)$ and $CO^{2+}(^1\Sigma^+, v=0)$ states (see Table II).

3. Channel (c,d): $C^{2+}+O$ and $O^{2+}+C$

The KECDs corresponding to reactions (c) and (d), obtained after an appropriate weighted subtraction of the pairs of KECDs corresponding to the (C^{2+}, e^-) events [(O^{2+}, e^-) respectively] and to the (C^{2+}, O^+, e^-) events [(C^+, O^{2+}, e^-) respectively], display no discrete structures. Because the statistics is low, we present the data in terms of one-dimensional E_e and KER distributions in Fig. 9. The electron energy distribution for both reactions [Figs. 9(b) and 9(d)] is continuously decreasing, suggesting direct double Auger decay, however, the slope of the distribution is much smaller than the one observed for reaction leading to (C^+/O^+) [Figs. 6(b) and 6(c)].

The intensity at $E_e = 10$ eV is only about half of the maximum of the distribution at low energy [below 1 eV for reaction (c) and about 2 eV for reaction (d)], therefore the discrimination conditions are more severe for these channels than for channels (a) and (b) in the reported experiment. The KER distribution for reaction (c) extends from 0 to 20 eV, with relative maxima at 9, 13.5, and 17 eV. Considering the CO^{2+} electronic states populated by double Auger decay in reaction (c) which dissociates into the $C^{2+}(^1S)+O(^3P)$ ground state limit at 45.75 eV, the observed structures correspond to CO^{2+} binding energy regions extending from 46 to 66 eV, centered at about 55, 59, and 63 eV. The fast electrons involved in the direct two electron decay, associated with the low electrons observed, would then belong to the D_5 region (50–60 eV) in the DES spectrum [42]. Similarly, the KER distribution for reaction (d) extends from 0 to 20 eV, with a broad maximum for KERs about 10 eV. For the CO^{2+} electronic states involved in reaction (d) which dissociate into the $C(^3P)+O^{2+}(^3P)$ ground state limit at 59.87 eV, the observed structures correspond to CO^{2+} binding energy regions

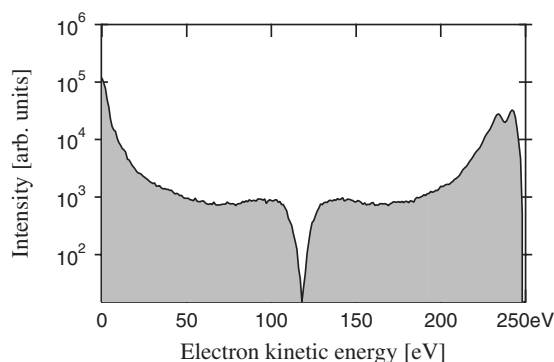


FIG. 10. Energy distribution spectrum of all electrons detected in coincidence, presented on a log scale. A filter was used to select electron pairs for which the sum of kinetic energies lies in the 220–250 eV range. The dip at the center of the distribution is an experimental artifact due to the detector dead time: two electrons arriving at the same time with the same energy are not counted in coincidence.

extending from 60 to 80 eV, centered at about 70 eV. The fast electrons corresponding to the low electrons observed would then participate to the flat higher energy distribution above peak D_5 [42]. These attributions are further discussed below.

B. Electron-electron coincidence

In order to probe in detail the mechanisms involving a cascade Auger decay, high energy resolution measurements are required. The magnetic bottle spectrometer provides a resolution $\Delta E/E \sim 1.6\%$ (limited to 10 meV below 1 eV) [10]. The energy resolution obtained for fast Auger electrons is on the contrary rather poor, ~ 4 eV, but is sufficient to obtain crucial information on sequential double Auger decay. Because ions are not detected in this experiment, no selection on the dissociation pathway is possible. However, coincidence measurements of two electrons limit the uncertainty on the dissociation pathways leading to the production of doubly charged species. We note that electronic decay via three-electrons emission after $C\ 1s \rightarrow 2\pi^*$ excitation is only 2% (Table IV of Hitchcock *et al.* [19]) compared to 29% for two-electrons emission. Consequently pollution of the data from three-electrons processes was neglected.

First, we show in Fig. 10 the energy distribution of all electrons detected in coincidence, from 0 to ~ 250 eV. Since no selection is made on the ions channel, the distribution shown in Fig. 10 includes the contribution of channels (a)–(d) and contains the sum of the energy distributions in Figs. 5–9. Figure 10 clearly shows that the distribution of electrons is continuous over the whole energy range and has a U-shape suggesting contribution from the direct double Auger. However, far ends also include the contribution from sequential processes, and it is the presence of electron emission at intermediate energy (30–200 eV) which is the clear signature of direct double Auger decay, since there are no electronic states of singly charged ion CO^+ that could explain these measured kinetic energies. Therefore direct double Auger decay represents at least 20% of the overall (direct + sequential) double Auger process by integrating this spec-

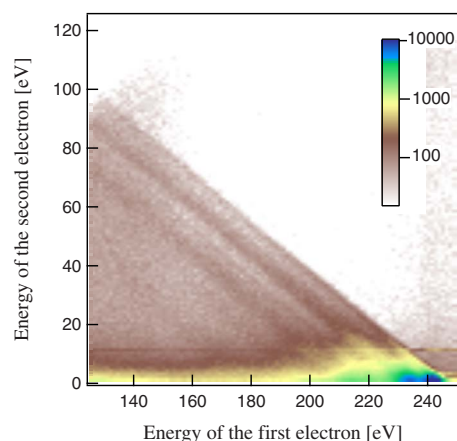


FIG. 11. (Color online) Electron-electron correlation map obtained at $h\nu = 287.4$ eV on the $C\ 1s \rightarrow 2\pi^*$. This map shows the intensity versus the energy of the slow and the fast electron. The energy sharing between the two electrons appears as diagonal lines in the map. The two-dimensional distribution is discretized with a 1.2 eV step. Intensity is coded in a log scale.

trum, if we assume a constant energy distribution for direct double Auger contribution taken in the energy region where no CO^+ states lies and neglect the characteristic U-shape discussed above. Figure 11 shows the electron-electron energy correlation diagram for the two Auger electrons after excitation at the $C\ 1s \rightarrow 2\pi^*$ resonance. Since the sum of both kinetic energies defines a given electronic CO^{2+} state in the case of double ionization in the Franck-Condon region, the energy distribution corresponding to a direct Auger decay to a specific CO^{2+} state appears as diagonal lines in the two-dimensional (2D) map. Most of the intensity in the 2D map is concentrated in the region with a slow electron in the (0, 20) eV energy range and a fast electron in the (230, 250) eV range, which corresponds to the ends of the electron energy distributions in Figs. 7, 8, and 10. Figure 12(a) shows an enlargement of this part of the (e^-, e^-) correlation diagram, where sequential Auger decay is observed. As it will be detailed in the following, the two broad vertical bands observed correspond to the decay of a CO^{++} intermediate [see Eq. (2)] while the thin horizontal lines reveal the autoionization of excited states O^* in atomic oxygen [see Eq. (3)].

Figure 12(b) shows the energy distribution of the fast electron. The two features can be assigned to electronic states of CO^{++} (D_4 and D_5 [45]) in agreement with Fig. 7 where two structures attributed to CO^{++} states are visible. The slight difference in the relative intensity of peaks D_4 and D_5 in both experiments can be attributed to the contribution of the (C^{2+}, O) channel, absent in Fig. 7, and which has been shown to be populated efficiently upon D_5 decay (see Sec. IV A 3), it can also originate in part from the lack of correction in the analyzer transmission in the high energy part in Fig. 7. The D_4/D_5 ratio was also found to be significantly larger in the noncoincident electron spectrum measured with HERMES [2.6 compared to 1.2 in Fig. 12(b)], in agreement with previous measurements of the resonant Auger spectra [42,45]. We attribute this to a high probability for the D_4 states to escape autoionization, and evolve to a dissociation path involving an ion and a neutral fragment.

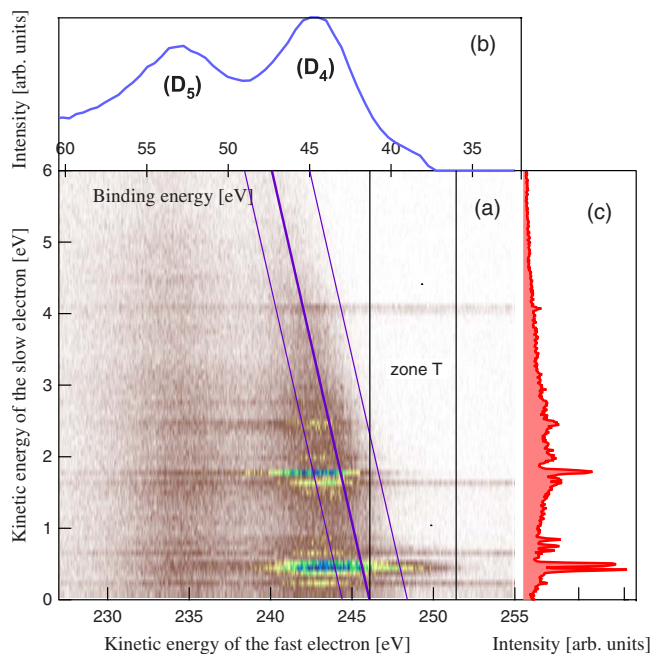


FIG. 12. (Color online) (a) Zoom of the electron-electron correlation map in Fig. 11, corresponding to energies of 0–6 eV for the slow electron and 227–255 eV for the fast electron (given in binding energy on the top of the graph). (b) On the top of the figure is shown (in blue) the energy distribution of the fast electron. In the 2D map the broad diagonal line indicates the CO^{2+} ground state. (c) On the right (in red) is shown the energy distribution of the slow electron, for electron pairs selected in a 4 eV band around this line. Structures at 0.2, 0.7, 1.6, and 4 eV in the 2D map are due to false coincidences which have been subtracted in the 1D projection.

In the two-dimensional map of Fig. 12, the broad diagonal line indicates the location of electron pairs associated with the formation of the stable CO^{2+} vibrational states. Figure 12(c) shows the energy distribution of the slow electrons along this diagonal line. Due to limited energy resolution on the fast electron, the sole contribution of the stable CO^{2+} vibrational states cannot be isolated in our data. Instead a 4 eV wide region across this diagonal line was selected. This region is represented in Fig. 12 by two diagonal lines. Thus Fig. 12(c) includes the contribution from CO^{2+} states in the 39–43 eV binding energy range. Sharp peaks are observed and are assigned to a fast dissociation into C^+ and O^* fragments followed by the autoionization of the atomic oxygen O^* . These atomic peaks lie on top of a broader feature (~ 4 eV wide) centered at around 2 eV kinetic energy, as shown in Fig. 12(c). From the two-dimensional map in Fig. 12, we can interpret this feature as the decay of the states D_4 . We attribute it to autoionization of the states D_4 in the Franck-Condon region, i.e., to molecular autoionization. Our measurements do not allow us to separate qualitatively this molecular contribution from direct double Auger decay: higher resolution for energetic electrons would be necessary. Therefore we cannot quantify the ratio between direct Auger and sequential decay due to molecular autoionization. Autoionization of the states D_4 can populate stable CO^{2+} vibrational states, providing some intensity along the diagonal line in Fig. 12, or dissociative CO^{2+} states of higher binding en-

ergies on the left of this diagonal line. This is in perfect agreement with the previous observations of a 2 eV wide peak in coincidence with CO^{2+} ions (Fig. 8, Sec. IV A 2) or with $\text{C}^+ + \text{O}^+$ fragments (process α in Fig. 5). As discussed previously the fixed 6.5 eV KER for the $\text{C}^+ + \text{O}^+$ α dissociation path should imply an energy sharing between the fast and slow electron giving a -1 slope in the (e^-, e^-) correlation map. This is not observed in Fig. 12, probably because of the poor resolution (4 eV) at high kinetic energy. The apparent -1 slope for the intensities along the diagonal line in Fig. 12 is attributed to an edge effect corresponding to the opening of the population of CO^{2+} states in the Franck-Condon region. From the (e^-, e^-) correlation map in Fig. 12, we observe that autoionization of the states D_4 also produces low energy electrons as low as 0 eV; a second maximum around 0.5 eV can be estimated below the sharp atomic lines. This leads to population of CO^{2+} states centered around 44.5 eV binding energy, which is consistent with process β described previously.

Autoionization of states D_5 leads to secondary low energy electrons of 0–5 eV kinetic energy. From Figs. 11 and 12, we rule out the autoionization of the D_5 states to the CO^{2+} ground states, in agreement with the previous electron-ion coincidence measurements. Instead, CO^{2+} states of higher binding energies, in the 60–48 eV energy range, are populated. These states can dissociate to $\text{C}^+ + \text{O}^+$ or $\text{C}^{2+} + \text{O}$ limits, as discussed in Sec. IV A.

The sum of the energies of the two electrons measured in coincidence is shown in Fig. 13(a). The kinetic energy scale was converted in binding energy: $E_{\text{binding}} = h\nu(287.4 \text{ eV}) - E_{\text{kinetic}}$. The spectrum extends from 38 eV up to 80 eV of binding energy and gives the energy distribution of the CO^{2+} states if we assume that they are populated in a Franck-Condon transition. In the case of a sequential decay, $\text{CO} + h\nu \rightarrow \text{CO}^+ + e_{\text{fast}}^- \rightarrow \text{CO}^{2+} + e_{\text{slow}}^- + e_{\text{fast}}^-$, the energy distributions of the individual electrons should represent the energy distribution of the intermediate electronic states.

To further investigate the decay dynamics, we analyzed the energy distribution of the slow electrons measured in coincidence with fast electrons for different energy regions of the spectrum in Fig. 13(a). Figure 13 shows three distinct energy selections we have made in (A) and the resulting energy distributions of slow electrons in (B)–(D). For CO^{2+} states in the 68–78 eV binding energy range, region (B), the slow Auger electron spectrum can be interpreted as the edge of a U-shaped distribution with a maximum at 0 eV characteristic of a direct double Auger decay. For CO^{2+} states in the 48–58 eV binding energy range, region (C), discrete peaks are observed on top of the direct double decay background. The third energy region (D) corresponds to the 39–43 eV binding energy range and the lower CO^{2+} states. The related slow electron spectrum is the one already displayed in Fig. 12(c), with a broad maximum at 2 eV, associated to the autoionization of the CO^{2+} states D_4 . Contribution of discrete peaks is here increased. Their origin can be understood in the bottom panel in Fig. 13. It corresponds to the distribution of low energy electrons, selected in region T of the two-dimension electron-electron correlation map in Fig. 12(a). Region T corresponds to a vertical cut of the coincidence map, different from the diagonal cuts (B)–(D). In this cut, the

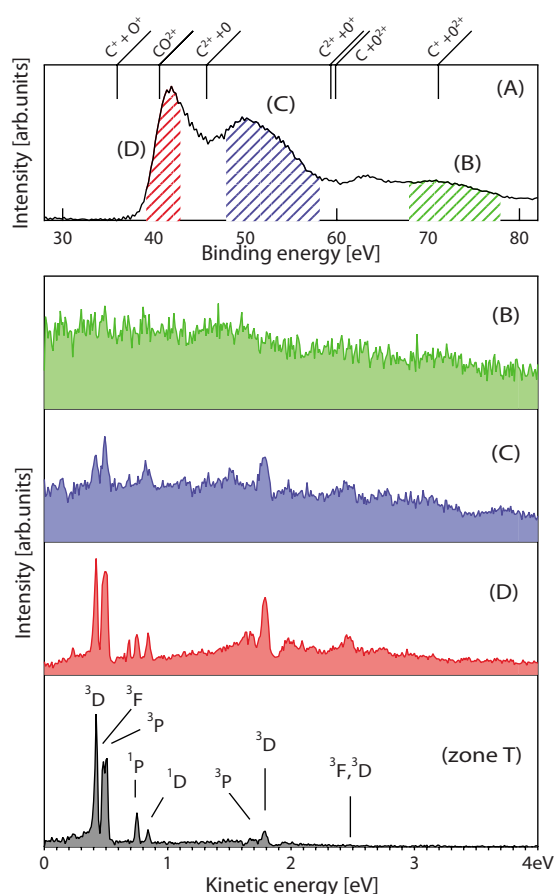


FIG. 13. (Color online) Energy distributions obtained from electron-electron coincidence measurements of the double Auger decay in CO after $C\ 1s \rightarrow 2\pi^*$ excitation at 287.4 eV. The sum of the two electron energies is shown in panel (A) on a binding energy scale and compared to the known thermochemical limits for fragments formation. Energy selections made are labeled (B), (C), and (D) and resulting energy distributions for the slow electrons are, respectively, displayed in panels (B)–(D). The lower panel displays the energy distribution of slow electrons selected in region T from Fig. 12—autoionizing states of atomic oxygen identified in the spectrum are indicated.

energy of the fast electron is fixed, which corresponds to the selection of a CO^{+*} intermediate state. Here, restriction to region T selects CO^{+*} states with binding energies in the 36–41.3 eV range. It is chosen to sit below the CO^{2+} threshold at 41.325 eV, and above the $C^+ + O^+$ thermochemical threshold at 35.98 eV corresponding to region I in Fig. 5. In the coincident slow Auger electron distribution in Fig. 13 (region T), the features associated to the formation of CO^{2+} states in the Franck-Condon region completely vanish and the spectrum shows only discrete lines. Only transitions that correspond to a sequential decay process take place in this energy range. As observed for lower photon energies for the first time by Becker *et al.* [55] and then by Hikosaka and Eland [49] these transitions correspond to autoionization of excited states of atomic oxygen (see Table III), after fragmentation of the CO^{+*} ion following the four-step sequential process:

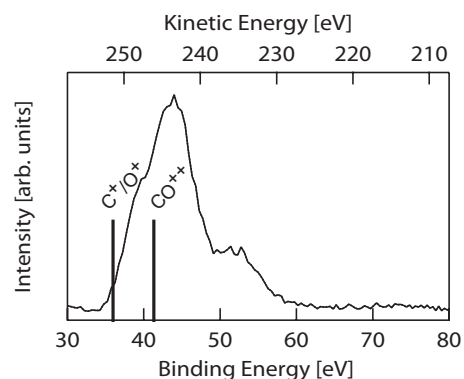


FIG. 14. Energy distribution obtained for the fast Auger electrons in coincidence with the atomic lines observed in the 0.32–0.52 eV energy range. The two vertical lines indicate the $C^+ + O^+$ threshold at 35.98 eV and the CO^{2+} threshold at 41.325 eV.

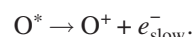
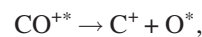


Figure 14 shows the energy distribution of the fast Auger electrons in coincidence with the oxygen atomic peaks observed in the 0.39–0.52 eV energy range shown in Fig. 13 (region T). This figure clearly demonstrates that the main CO^{+*} electronic states leading to the autoionization of atomic oxygen have binding energies above the CO^{2+} threshold (see discussion of region II of the KECD in Sec. I). These states created after spectator decay are dissociative and all have an electron in the 2π orbital. During dissociation the electron in the 2π orbital is transferred to the neutral oxygen atom, to a superexcited Rydberg state with a (2P) or (2D) core, that lies above the $O^+(^4S)$ ionization limit of the atomic oxygen and can then undergo subsequent autoionization. This sequential processes finally leads to $C^+(^2P) + O^+(^4S)$ ground states of the ionic fragments lying at 35.98 eV above the CO ground state.

The shape of the spectrum in Fig. 14 recalls that of Fig. 12(b), but CO^{+*} states (D_4) and (D_5) are found to present a different probability to lead to O^* autoionization. The D_5 components also appear truncated in Fig. 14, probably due to the different behavior of unresolved states which could be separated with a better resolution on the fast electron. Finally, the significant probability of atomic autoionization, found for CO^{+*} states lying just above the C^+/O^+ limit at 35.98 eV, below the CO^{2+} threshold is confirmed. These states lead to a low KER and contribute to region I of the KECD plot in Figs. 6(a).

Many studies have already identified this decay channel as a major contributory process in the formation of $C^+ + O^+$ ions after valence photoionization below the CO^{2+} threshold [49,52,55,56]. The spectrum obtained in Fig. 13 (region T) compares to the spectrum obtained recently by Hikosaka and Eland [49] after photoionization at $h\nu=40.814$ eV. The only difference is the CO^{+*} ion is here created indirectly by non-radiative relaxation of the $C\ 1s$ core-excited molecule.

Becker *et al.* [55] recalled that the two processes, relaxation of the CO^{+*} ion forming CO^{2+} that dissociates to $\text{C}^+ + \text{O}^+$ or dissociation of the CO^{+*} ion followed by relaxation of the atomic O^* fragment, differ only from each other by the interatomic distance where the electronic decay takes place. Fast dissociation after core excitation was identified for the first time in HBr [57] and later in many molecules. In the case of CO, the potential energy curve of the intermediate $(2\sigma)^{-1}(2\pi)^{+1}$ state is not dissociative. The dynamics of the core excitation does not influence much the decay and we observe basically the same subsequent sequential decay observed after direct photoionization just below the CO^{2+} formation threshold. However, it is remarkable that through this process, the localized excitation of the C $1s$ core orbital leads to a delocalization of the decay process via the delocalized 2π valence orbital, and to autoionization in the atomic oxygen fragment. Contrary to the observation made in [55], and not confirmed by later experiments [49], we do not observe peaks corresponding to autoionization in the atomic carbon fragment at the resonance.

V. CONCLUSION

We have studied double Auger decay following core-shell excitation of a molecule, namely C $1s \rightarrow 2\pi^*$ excitation of carbon monoxide. Using three complementary coincident techniques, two distinct mechanisms have been observed and assigned to direct and sequential double Auger decay. Direct double Auger decay was characterized through the continuous energy sharing between the two Auger electrons emitted simultaneously in the process. This gives rise to a characteristic U-shaped energy distribution with a nonzero intensity in an energy region where no CO^+ states are found. This is

illustrated by the electron-electron coincident measurements covering the whole electron energy range. The high resolution electron-electron data also allows one to identify unambiguously the sequential process involving the dissociation of the molecular ion CO^{+*} followed by autoionization of the oxygen fragment. The contribution of each double ionization channels, leading to $\text{C}^+ + \text{O}^+$, CO^{2+} , $\text{C}^{2+} + \text{O}$, and $\text{O}^{2+} + \text{C}$, and the production of an associated low energy electron ($E_e < 15$ eV) have been resolved using the vector correlation method. This method also allows one to characterize a specific contribution from molecular autoionization channels populated after decay of CO^{+*} states and assigned to specific binding energy regions. These measurements give access to the molecular frame slow-Auger electron angular distributions that will be reported separately. A higher resolution in the analysis of the fast electrons, for electron-electron and electron-ion coincidence experiments, and the low energy electrons in the vector correlation experiment, is needed for a higher degree of understanding of these complex decay mechanisms.

ACKNOWLEDGMENTS

Financial support of PICS by CNRS is gratefully acknowledged. This work was also supported by the European Community through the I3 initiative on Synchrotrons and FELs. The project was approved by the Bessy committee program and was supported in part by the European Community, Research Infrastructure Action under the FP6 "Structuring European research Area" Programme (Contract No. R II 3-CT-2004-506008). The authors thank Thierry Marin and Bertrand Pilette, as well as the staff of the synchrotron radiation facilities LURE, Max II, and Bessy II for their support.

-
- [1] M. O. Krause, *J. Phys. Chem. Ref. Data* **8**, 307 (1979).
 [2] T. A. Carlson and M. O. Krause, *Phys. Rev. Lett.* **14**, 390 (1965).
 [3] T. A. Carlson and M. O. Krause, *Phys. Rev. Lett.* **17**, 1079 (1966).
 [4] P. Lablanquie, S. Sheinerman, F. Penent, R. I. Hall, M. Ahmad, Y. Hikosaka, and K. Ito, *Phys. Rev. Lett.* **87**, 053001 (2001).
 [5] J. Viehhaus, S. Cvejanovic, B. Langer, T. Lischke, G. Prümper, D. Rolles, A. V. Golovin, A. N. Grum-Grzhimailo, N. M. Kabachnik, and U. Becker, *Phys. Rev. Lett.* **92**, 083001 (2004).
 [6] J. Viehhaus, A. N. Grum-Grzhimailo, N. Kabachnik, and U. Becker, *J. Electron Spectrosc. Relat. Phenom.* **141**, 121 (2004).
 [7] F. Penent, J. Palaudoux, P. Lablanquie, L. Andric, R. Feifel, and J. H. D. Eland, *Phys. Rev. Lett.* **95**, 083002 (2005).
 [8] J. Viehhaus, M. Braune, S. Korica, A. Reinköster, D. Rolles, and U. Becker, *J. Phys. B* **38**, 3885 (2005).
 [9] V. Jonauskas, L. Partanen, S. Kučas, R. Karazija, M. Huttula, S. Aksela, and H. Aksela, *J. Phys. B* **36**, 4403 (2003).
 [10] P. Lablanquie, L. Andric, J. Palaudoux, U. Becker, M. Braune, J. Viehhaus, J. H. D. Eland, and F. Penent, *J. Electron Spectrosc. Relat. Phenom.* **156–158**, 5157 (2007).
 [11] U. Becker, T. Prescher, E. Schmidt, B. Sonntag, and H.-E. Wetzel, *Phys. Rev. A* **33**, 3891 (1986).
 [12] P. A. Heimann, D. W. Lindle, T. A. Ferret, S. H. Liu, L. J. Medhurst, M. N. Piancastelli, D. A. Shirley, U. Becker, H. G. Kerkoff, B. Langer, D. Szostak, and R. Wehlitz, *J. Phys. B* **20**, 5005 (1987).
 [13] U. Becker, D. Szostak, M. Kupsch, H. G. Kerkoff, B. Langer, and R. Wehlitz, *J. Phys. B* **22**, 749 (1989).
 [14] T. Lebrun, M. Lavollée, M. Simon, P. Morin, and P. Lablanquie, *J. Chem. Phys.* **98**, 2534 (1993).
 [15] M. Simon, P. Morin, P. Lablanquie, M. Lavollée, K. Ueda, and N. Kosugi, *Chem. Phys. Lett.* **238**, 42 (1995).
 [16] M. Lavollée and V. Brems, *J. Chem. Phys.* **110**, 918 (1999).
 [17] K. Ueda, *Surf. Rev. Lett.* **9**, 21 (2002).
 [18] N. Saito, F. Heiser, O. Hemmers, A. Hempelmann, K. Wieliczek, J. Viehhaus, and U. Becker, *Phys. Rev. A* **51**, R4313 (1995).
 [19] A. P. Hitchcock, P. Lablanquie, P. Morin, E. LizonALugrin, M. Simon, P. Thiry, and I. Nenner, *Phys. Rev. A* **37**, 2448 (1988).
 [20] A. Lafosse, J. C. Brenot, A. Golovin, P. M. Guyon, K. Hoerjrup, J. C. Houver, M. Lebech, and D. Dowek, *J. Chem. Phys.* **114**, 6605 (2001).

- [21] M. Lebeck, J. C. Houver, and D. Doweck, *Rev. Sci. Instrum.* **73**, 1866 (2002).
- [22] C. Miron, M. Simon, N. Leclercq, and P. Morin, *Rev. Sci. Instrum.* **68**, 3728 (1997).
- [23] D. Céolin, C. Miron, M. Simon, and P. Morin, *J. Electron Spectrosc. Relat. Phenom.* **141**, 171 (2004).
- [24] J. H. D. Eland, O. Vieuxmaire, T. Kinugawa, P. Lablanquie, R. I. Hall, and F. Penent, *Phys. Rev. Lett.* **90**, 053003 (2003).
- [25] R. Guillemin, E. Shigemasa, K. Le Guen, D. Céolin, C. Miron, N. Leclercq, P. Morin, and M. Simon, *Phys. Rev. Lett.* **87**, 203001 (2001).
- [26] M. R. Weiss, R. Follath, K. J. S. Sawhney, F. Senf, J. Bahrtdt, W. Frentrup, A. Gaupp, S. Sasaki, M. Scheer, H. C. Mertins, D. Abramsohn, F. Schäfers, W. Kuch, and W. Mahler, *Nucl. Instrum. Methods Phys. Res. A* **467**, 449 (2001).
- [27] K. J. S. Sawhney, F. Senf, M. Scheer, F. Schäfers, J. Bahrtdt, A. Gaupp, and W. Gudat, *Nucl. Instrum. Methods Phys. Res. A* **390**, 395 (1997).
- [28] W. B. Li, R. Montuoro, J. C. Houver, L. Journal, A. Haouas, M. Simon, R. R. Lucchese, and D. Doweck, *Phys. Rev. A* **75**, 052718 (2007).
- [29] M. Richard-Viard, A. Delboulbé, and M. Vervloet, *Chem. Phys.* **209**, 159 (1996).
- [30] M. Bässler, J.-O. Forsell, O. Björneholm, R. Feifel, M. Jurvan-suu, S. Aksela, S. Sundin, S. L. Sorensen, R. Nyholm, A. Aus-meets, and S. Svensson, *J. Electron Spectrosc. Relat. Phenom.* **101–103**, 953 (1999).
- [31] K. Le Guen, D. Céolin, R. Guillemin, C. Miron, N. Leclercq, M. Bougeard, M. Simon, P. Morin, A. Mocellin, F. Burmeister, A. Naves de Brito, and S. L. Sorensen, *Rev. Sci. Instrum.* **73**, 3885 (2002).
- [32] R. W. Wetmore, R. J. Le Roy, and R. K. Boyd, *J. Phys. Chem.* **88**, 6318 (1984).
- [33] C. Tian and C. R. Vidal, *Phys. Rev. A* **59**, 1955 (1999).
- [34] P. Lablanquie, J. Delwiche, M.-J. Hubin-Franskin, I. Nenner, P. Morin, K. Ito, J. H. D. Eland, J.-M. Robbe, G. Gandara, J. Fournier, and P. G. Fournier, *Phys. Rev. A* **40**, 5673 (1989).
- [35] F. Penent, R. I. Hall, R. Panajotovic, J. H. D. Eland, G. Chappelier, and P. Lablanquie, *Phys. Rev. Lett.* **81**, 3619 (1998).
- [36] G. Dawber, A. G. McConkey, L. Avaldi, M. A. MacDonald, G. C. King, and R. I. Hall, *J. Phys. B* **27**, 2191 (1994).
- [37] L. S. Cederbaum, P. Campos, F. Tarantelli, and A. Sgamellotti, *J. Chem. Phys.* **95**, 6634 (1991).
- [38] M. Hochlaf, R. I. Hall, F. Penent, H. Kjeldsen, P. Lablanquie, M. Lavollée, and J. H. D. Eland, *Chem. Phys.* **207**, 159 (1996).
- [39] M. Lundqvist, P. Baltzer, D. Edvardsson, L. Karlsson, and B. Wannberg, *Phys. Rev. Lett.* **75**, 1058 (1995).
- [40] N. Correia, A. Flores-Riveros, H. Ågren, K. Helenelund, L. Asplund, and U. Gelius, *J. Chem. Phys.* **83**, 2035 (1985).
- [41] L. H. Andersen, J. H. Posthumus, O. Vahtras, H. Ågren, N. Elander, A. Nunez, A. Scrinzi, M. Natiello, and M. Larsson, *Phys. Rev. Lett.* **71**, 1812 (1993).
- [42] W. Eberhardt, E. W. Plummer, I. Whan Lyo, R. Reininger, R. Carr, W. K. Ford, and D. Sondericker, *Aust. J. Phys.* **39**, 633 (1986).
- [43] S. K. Botting and R. R. Lucchese, *Phys. Rev. A* **56**, 3666 (1997).
- [44] M. N. Piancastelli, M. Neeb, A. Kivimäki, B. Kempgens, H. M. Köppe, K. Maier, A. M. Bradshaw, and R. F. Fink, *J. Phys. B* **30**, 5677 (1997).
- [45] O. Hemmers, F. Heiser, J. Vieffhaus, K. Wieliczek, and U. Becker, *J. Phys. B* **32**, 3769 (1999).
- [46] O. Hemmers, F. Heiser, J. Eiben, R. Wehlitz, and U. Becker, *Phys. Rev. Lett.* **71**, 987 (1993).
- [47] P. Baltzer, M. Lundqvist, B. Wannberg, L. Karlsson, M. Larsson, M. A. Hayes, J. B. West, M. R. F. Siggel, A. C. Parr, and J. L. Dehmer, *J. Phys. B* **27**, 4915 (1994).
- [48] F. Penent, J. P. Grouard, J. L. Montmagnon, and R. I. Hall, *J. Phys. B* **23**, 2105 (1990).
- [49] Y. Hikosaka and J. H. D. Eland, *Chem. Phys.* **299**, 147 (2004).
- [50] R. E. Huffman, J. C. Larrabee, and Y. Tanaka, *J. Chem. Phys.* **46**, 2213 (1967).
- [51] V. Čermák and J. Šrámek, *J. Electron Spectrosc. Relat. Phenom.* **2**, 97 (1973).
- [52] D. B. Thompson, G. Dawber, N. Gulley, M. A. MacDonald, and G. C. King, *J. Phys. B* **30**, L147 (1997).
- [53] Th. Weber, O. Jagutzki, M. Hattass, A. Staudte, A. Nauert, L. Schmidt, M. H. Prior, A. L. Landers, A. Bräuning-Demian, H. Bräuning, C. L. Cocke, T. Osipov, I. Ali, R. Díez Muiño, D. Rolles, F. J. García de Abajo, C.S. Fadley, M. A. VanHove, A. Cassimi, H. Schmidt-Böcking, and R. Dörner, *J. Phys. B* **34**, 3669 (2001).
- [54] N. Saito, F. Heiser, O. Hemmers, K. Wieliczek, J. Vieffhaus, and U. Becker, *Phys. Rev. A* **54**, 2004 (1996).
- [55] U. Becker, O. Hemmers, B. Langer, A. Menzel, R. Wehlitz, and W. B. Peatman, *Phys. Rev. A* **45**, R1295 (1992).
- [56] U. Becker and R. Wehlitz, *J. Electron Spectrosc. Relat. Phenom.* **67**, 341 (1994).
- [57] P. Morin and I. Nenner, *Phys. Rev. Lett.* **56**, 1913 (1986).